# Author's Accepted Manuscript

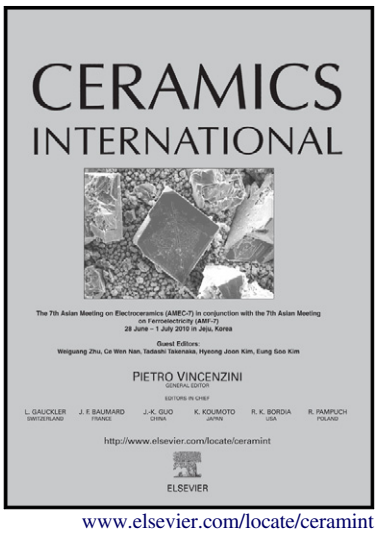


www.elsevier.com/locate/ceramint

The influence of $Fe_2O_3$ doping on the pore structure and mechanical strength of $TiO_2$-containing alumina obtained by freeze-casting

Alysson M.A. Silva, Eduardo H.M. Nunes, Douglas F. Souza, Dana L. Martens, João C.Diniz da Costa, Manuel Houmard, Wander L. Vasconcelos

PII: S0272-8842(15)01307-3
DOI: http://dx.doi.org/10.1016/j.ceramint.2015.07.021
Reference: CERI10905

To appear in: *Ceramics International*

Received date: 22 May 2015
Revised date: 2 July 2015
Accepted date: 3 July 2015

Cite this article as: Alysson M.A. Silva, Eduardo H.M. Nunes, Douglas F. Souza, Dana L. Martens, João C.Diniz da Costa, Manuel Houmard, Wander L. Vasconcelos, The influence of $Fe_2O_3$ doping on the pore structure and mechanical strength of $TiO_2$-containing alumina obtained by freeze-casting, *Ceramics International,* http://dx.doi.org/10.1016/j.ceramint.2015.07.021

# THE INFLUENCE OF $Fe_2O_3$ DOPING ON THE PORE STRUCTURE AND MECHANICAL STRENGTH OF $TiO_2$-CONTAINING ALUMINA OBTAINED BY FREEZE-CASTING

Alysson M.A. Silva[(1)*], Eduardo H.M. Nunes[(1)**], Douglas F. Souza[(1)], Dana L. Martens[(2)], João C. Diniz da Costa[(2)], Manuel Houmard[(3)], Wander L. Vasconcelos[(1)***]

(1) Department of Metallurgical and Materials Engineering,
Federal University of Minas Gerais – UFMG
Avenida Presidente Antônio Carlos, 6627, Campus UFMG, Belo Horizonte, MG,
CEP: 31270-901, Escola de Engenharia, bloco 2, sala 2230 – Brasil

(2) The University of Queensland, FIMLab – Films and Inorganic Membrane Laboratory, School of Chemical Engineering, Brisbane, Queensland, 4072, Australia

(3) Department of Materials Engineering and Civil Construction,
Federal University of Minas Gerais – UFMG
Avenida Presidente Antônio Carlos, 6627, Campus UFMG, Belo Horizonte, MG,
CEP: 31270-901, Escola de Engenharia, bloco 1, sala 3304 – Brasil

* alysson_fisica@yahoo.com.br

** eduardohmn@gmail.com

*** wlv@demet.ufmg.br

**ABSTRACT**

This work investigated $TiO_2/Fe_2O_3$ doped alumina prepared by the freeze-casting technique and using camphene as the solvent. Dendritic pores were formed in the $TiO_2$ doped alumina, a structure conferred by the frozen camphene. Contrary to this trend, further $Fe_2O_3$ doping of $TiO_2$-containing alumina resulted in the formation of non-dendritic structures. This behavior was attributed to the higher density of $\alpha$-$Fe_2O_3$ (5.24 g $cm^{-3}$) when compared to $\alpha$-$Al_2O_3$ (3.95 g $cm^{-3}$) and anatase $TiO_2$ (3.89 g $cm^{-3}$), which reduced critical solidification front velocity, thus forming material with different pore shape. $Fe_2O_3$ doping also improved the densification of $TiO_2$-alumina and inhibited the formation of cracks, reflected by superior mechanical strength with best results ~150% higher for 10% $Fe_2O_3$ loaded samples as compared to $TiO_2$-alumina samples.

**KEYWORDS:** A. Porosity; B. Strength; C. $Al_2O_3$; D. $TiO_2$.

## 1. INTRODUCTION

The freeze casting technique has been gathering research interest due to its versatility in the preparation of tailored porous materials. This technique has benefited a number of applications including biomaterials derived from hydroxyapatite scaffolds for bone tissue engineering [1], unidirectional coating using nano-titania particles [2], iron oxide scaffolds [3], porous alumina substrates [4], lightweight and mechanically reliable materials with tailored pore frameworks [5], and hierarchical perovskite structures for

oxygen separation from air [6]. A common principle of this technique is the use of stable colloidal solutions in which the solvent solidifies during the cooling step. This is a very quick process, and cooling is almost instantaneous, resulting in a moving solidification front where the colloidal particles are rejected from the moving solidification front. In this process, the particles are entrapped between the growing solvent crystals [7]. As this solidification front growth can be directed into a single direction, this technique confers pore tailoring upon solvent sublimation and sintering.

Porous alumina is attractive in a large number of applications due to good compatibility with other inorganic materials, mechanical properties and low cost. For instance, porous alumina protective layers by spray coating [8, 9], foam materials [10, 11], and membrane substrates generally made by extrusion for microfiltration [12, 13], nanofiltration [14, 15], gas separation [16-18], oil/water separation [19, 20] and desalination [21-23]. The freeze casting technique also proved excellent for the production of porous alumina substrates. This is particularly important in membrane application where freeze casting substrates offer reduced resistance to gas transport as compared to conventional porous ceramic production methods. Hence, the structural development of alumina based freeze casting has been reported based on controlling the lamellar pore structure [24] by symmetrical channel arrangements along the radial axis [25]. Furthermore, a number of solvents have been investigated towards freeze casting structure formation in addition to water, including tert-butanol [4], naphthalene [26], polyether glycol [27], glycerol [28] and camphene [29, 30] among many other examples.

The mechanical properties of porous alumina substrates are also important and doping with different metal oxides is a strategy employed accordingly. For instance, it is well known that doping titania into alumina tends to form an aluminum titanate ($Al_2TiO_5$) phase with superior mechanical strength than alumina [31]. Recently, it was reported that $TiO_2$ doping with loadings above 4 wt% reduced the mechanical strength in freeze-cast alumina which was associated with the formation of microcracks [32]. Hence, metal oxide doping must be controlled to a point where it is no longer beneficial. $SiO_2$, $Fe_2O_3$ and MgO [33-36] have also been used as doping agents into alumina in attempting to increase the poor mechanical strength related to an extensive microcracking.

In this work we investigated the effect of $Fe_2O_3$ doping on the properties of $TiO_2$-alumina samples obtained by freeze-casting. As far as we know, this is the first attempt to incorporate $TiO_2$ and $Fe_2O_3$ into freeze-cast alumina, thus allowing the examination of novel tailored pore structures coupled with mechanical properties. This study is supported by a series of experimental tests including X-ray diffraction (XRD), Fourier transform infrared spectroscopy (FTIR), scanning electron microscopy (SEM), electron dispersive spectroscopy (EDS), Archimedes method, and X-ray microtomography (μ-CT). The cold crushing strength of the samples prepared in this work was also evaluated.



## 2. MATERIALS AND METHODS

### 2.1 SYNTHESIS

The freeze-cast samples were obtained following a method as published elsewhere [32]. Briefly, a solution of Texaphor 963 (Cognis, Southampton Hampshire, UK) and camphene (Aldrich / ≥ 95%) was prepared at 60 °C, where CT3000SG alumina particles (Almatis, Brazil / ≥ 99%) were then added under vigorous stirring. Texaphor 963 is a 50 wt% solution of an electroneutral salt of polycarboxylic acid with amine derivatives, whereas camphene is a bicyclic monoterpene with molecular formula $C_{10}H_{16}$. The as-prepared slurry was kept under sonication for 15 min, followed by sequential addition of $TiO_2$ (anatase / Sigma / ≥ 99%) and $\alpha$-$Fe_2O_3$ (Baker Chemicals / 99.4%) to this slurry. The $TiO_2$ loading was kept at 4 wt% of the solid concentration, whereas the $Fe_2O_3$ concentration ranged from 2.5 to 10 wt%. Blank samples containing pure alumina were also prepared for comparison purposes. The Texaphor 963 loading was kept at 1.8 wt% of the alumina concentration. The solid concentration in the slurries was kept constant at 25 vol%.

Subsequently, the slurries were poured into a freeze casting rig containing a high thermal conductivity copper plate and a polytetrafluoroethylene (PTFE) mold. The bottom side of the mold was in contact with the copper plate at ~77K (e.g. liquid nitrogen) while the top side of the mold was open to atmospheric conditions. The slurry was poured into the mold and due to a high temperature gradient, it created a front freezing the camphene crystals in the vertical orientation from the bottom to the top side of the mold. The removal of camphene was carried out in air at room temperature for at least 3 days. The samples were then calcined in air at 1500 °C for 2 h using a temperature-controlled Thermolab furnace at a heating rate of 2 °C $min^{-1}$.

## 2.2 CHARACTERIZATION

The starting powders used in this work were examined by laser granulometry with a CILAS 1064 laser granulometer. The porosity of the sintered samples was measured by the Archimedes method. The sample's shrinkage was evaluated taking into account their diameter before and after the heat treatment step. XRD was carried out using a PHILIPS-PANALYTICAL PW 1710 diffractometer, with Cu Kα radiation and operating at 40 kV and 30 mA. XRD patterns were taken in the range of 10-80° (2θ), using a step size of 0.06°. The identification of the crystalline phases was performed using the XPert Plus software. FTIR was used to analyze samples prepared as pellets with KBr and examined in a PERKIN-ELMER Frontier spectrometer. The spectra were taken from 4000 to 400 $cm^{-1}$, with a resolution of 4 $cm^{-1}$ and 128 scans.

SEM was carried out in a FEI Quanta 200F field emission scanning electron microscope (FESEM) using accelerating voltages from 10 to 20 kV. The samples were embedded in epoxy resin, ground, and polished with diamond paste. Subsequently, the samples were placed in an ultrasonic bath with acetone, dried under hot air, and sputter-coated with a 5 nm thick gold layer. Compositional analyses were measured using a NORAN EDS system available in the microscope. μ-CT was carried out with a SKYSCAN 1172 high-resolution micro system. These tests were conducted using 100 kV X-ray voltage and a 0.5 mm thick aluminum filter. Three-frame averaging and a rotation step of 0.30° were used, covering a view of 180°. Smoothing and beam-hardening correction were applied to suppress noise and beam hardening artifacts. Cold crushing tests were carried out at room temperature using a CONTENCO HD-20T servo-controlled press.

## 3. RESULTS AND DISCUSSION

Figure 1 depicts the particle size distribution of the starting powders used in this study. It is observed that the particle size distribution of α-$Fe_2O_3$ (0.85 μm) and $TiO_2$ (0.9 μm) is shifted towards larger particle sizes when compared to α-$Al_2O_3$ (0.8 μm). These particle sizes are within the values generally used in freeze casting process, as the particle size tends not to interfere in the formation of the camphene structure. The latter provides the porous structure during the freeze-casting method. Figure 2 shows XRD patterns of samples obtained in this work. It is observed that α-$Al_2O_3$ is the major phase in these materials. β-$Al_2TiO_5$ is clearly observed in $TiO_2$-containing samples since the formation of this phase occurs at temperatures above 1280 °C as per equation (1), associated with the transport of aluminum ions through $TiO_2$ [37]. The XRD patterns also reveal that the higher the concentration of α-$Fe_2O_3$, the more pronounced are the diffraction lines ascribed to $Fe_2TiO_5$. These results suggest the formation of $Fe_2TiO_5$ as per equation (2), related to the diffusion of $TiO_2$ into α-$Fe_2O_3$ [38]. It is also observed at the diffraction line 2θ ~50° that the formation of $Al_{2-2x}Fe_{2x}TiO_5$ (with $x$ range from 0 to 1) took place in samples prepared with $Fe_2O_3$ loadings above 7.5 wt%. This reaction is described in equation (3) [39].

$$\alpha\text{-}Al_2O_3 + TiO_2 \rightarrow \beta\text{-}Al_2TiO_5 \ . \quad (1)$$

$$Fe_2O_3 + TiO_2 \rightarrow Fe_2TiO_5 \ . \quad (2)$$

$$Al_2TiO_5 + xFe_2O_3 \rightarrow Al_{2-2x}Fe_{2x}TiO_5 + xAl_2O_3 \ . \quad (3)$$

Figure 3 displays the FTIR spectra of the as-prepared materials together with the starting powders for comparison purposes. The bands at 460, 490, 610, and 645 $cm^{-1}$ were ascribed to $AlO_6$ octahedra [40, 41]. The shoulder at 545 $cm^{-1}$ was assigned to the presence of $\alpha$-$Fe_2O_3$ and anatase $TiO_2$. It is observed that the higher the concentration of $\alpha$-$Fe_2O_3$, the more pronounced is this shoulder. Some authors have ascribed bands at ~545 $cm^{-1}$ to Fe-O bonds [42, 43], thus coinciding with the broad absorption band also at ~545 $cm^{-1}$ for the $\alpha$-$Fe_2O_3$ powder used in this study. The band at 780 $cm^{-1}$ was assigned to $AlO_4$ units [44-46]. A band at 1085 $cm^{-1}$ is clearly observed in the spectra of $Fe_2O_3$-containing samples, which became more pronounced when the $\alpha$-$Fe_2O_3$ concentration increased. This feature has not been ascribed to a specific iron-related compound and could be associated with a compound formed in alumina after the co-doping of $TiO_2$ and $\alpha$-$Fe_2O_3$ ($Fe_2TiO_5$ / $Al_{2-2x}Fe_{2x}TiO_5$). It was not possible to identify the bands related to Ti-O bonds because they are masked by those associated with Al-O bonds.

The SEM micrographs of $TiO_2$-containing alumina in Fig. 4 clearly show the formation of dendritic pores. As camphene tends to solidify in a dendritic fashion [47], its use as the solvent in freeze-casting leads to materials with dendritic pore channels [48-50]. Micrograph 4B shows that camphene dendrites grew macroscopically with a preferential orientation similar to the freezing direction. Fast freezing rates such as those used in this work usually lead to fine pore structures in freeze-cast materials. Figure 5 depicts SEM micrographs of materials obtained by the co-doping of $TiO_2$ and $\alpha$-$Fe_2O_3$ into $\alpha$-$Al_2O_3$. Dendritic pores are no longer observed in these samples. It is well established that in freeze-casting the slurry particles are pushed away by the solidification front and trapped between the growing solvent crystals. The critical

solidification front velocity ($v_c$) for particle trapping can be estimated by equation (4) [51, 52]:

$$v_c = \frac{\rho_1}{9\eta\rho_s}\left[-\frac{B}{2\pi Dd_0} - gDd_0\left(\rho_p - \rho_1\right)\right] \quad , \tag{4}$$

where D represents the particle diameter, g the gravitational constant, B a negative constant, $\eta$ the viscosity of the liquid phase, $d_0$ the minimal distance between the particle and solidification front, $\rho_p$ the particle density, $\rho_s$ and $\rho_l$ the densities of the solid and liquid phases, respectively. The particle engulfment occurs when the solidification velocity is higher than this critical value. Equation (4) indicates that the critical solidification front velocity is inversely proportional to the particle density. Since the density of $\alpha$-$Fe_2O_3$ (5.24 g $cm^{-3}$) is significantly higher than those of $\alpha$-$Al_2O_3$ (3.95 g $cm^{-3}$) and anatase $TiO_2$ (3.89 g $cm^{-3}$), its addition to the slurry leads to a reduced critical solidification front velocity. As a consequence, the formation of dendritic pores was inhibited as evidenced in the SEM micrograph shown in Figure 5.

Figure 6 depicts SEM micrograph and EDS spectra of $TiO_2$/$Fe_2O_3$-containing alumina. The EDS signals show that the dark-gray regions were ascribed to Al, whereas light-gray areas exhibited signals associated with Al, Ti, and Fe. These results correlate well to the XRD patterns in Figure 2 and are attributed to the presence of $\beta$-$Al_2TiO_5$, $Fe_2TiO_5$, and $Al_{2-2x}Fe_{2x}TiO_5$ in the light-gray regions since they show a higher atomic number than alumina. The EDS signal ascribed to C is associated with the epoxy resin in which samples were embedded before the SEM tests. From Figures 5 and 6, it can be

observed that the light-gray regions are highly dispersed within the sample microstructure.

It is interesting to observe in Figure 7 that the $Fe_2O_3$ doping greatly reduced cracking formation. For instance, all samples containing alumina and titania resulted in cracks, some of them displaying several deep cracks. However, the samples containing alumina and titania plus $Fe_2O_3$ resulted in single micro-cracks only. These results strongly suggest that $Fe_2O_3$ doping assisted in the sintering process and promoted a superior matching between the compounds formed. $Fe_2TiO_5$ is an isostructural compound that might decrease the formation of cracks resulting from the thermal expansion mismatch of $\alpha$-$Al_2O_3$ and $\beta$-$Al_2TiO_5$ [53, 54].

Figure 8 exhibits the porosity and shrinkage of samples prepared in this work as a function of the $\alpha$-$Fe_2O_3$ concentration. The trends are quite clear in the sense that pure alumina showed a higher porosity and lower shrinkage than the $TiO_2$-containing sample. This behavior is associated with a more effective sintering of alumina when titania is added into its structure, in line with enhanced densification and grain growth [55-58]. The initial doping of 2.5 wt% $Fe_2O_3$ loading to the $TiO_2$-containing sample seems to not alter both the porosity and shrinkage. However, when $Fe_2O_3$ loadings exceeded 2.5 wt%, samples with lower porosities and higher shrinkages were obtained. This finding is in line with the results reported elsewhere [59]. Archimedes tests also revealed that the materials obtained in this study show similar total and open porosities. This behavior suggests that they exhibit highly interconnected pore structures.

The cold crushing strength results in Figure 9 shows that $TiO_2$-containing alumina strength was slightly higher than that of pure alumina. The initial doping of 2.5 wt% $Fe_2O_3$ did not alter the cold crushing strength specimens though higher mechanical strengths were obtained when the $Fe_2O_3$ loading increased to and above 5 wt%. The cold crushing strength as a function of the porosity decreased as porosity increased to ~27%, and from there on the crushing strength was almost independent of porosity. Therefore, $Fe_2O_3$ doping improved the densification of the $TiO_2$-containing alumina and also inhibited the formation of cracks resulting from the $\beta$-$Al_2TiO_5$ phase. This behavior was also attributed to the increase of the cold crushing strength by ~150% for 10% $Fe_2O_3$ loaded samples as compared to $TiO_2$-alumina samples. It is worth mentioning that, in spite of the high porosity of the samples tested; they withstood the cold crushing tests (up to fracture) and did not crumble upon handling.

## 4. CONCLUSIONS

Laser granulometry tests revealed that the starting powders used in this work show mean particle diameters below 1 μm, which suggests that they do not interfere in the formation of the camphene structure. XRD patterns showed that $\alpha$-$Al_2O_3$ was the major phase in the samples and $\beta$-$Al_2TiO_5$ was observed in $TiO_2$ doped materials. It was noticed that the higher the concentration of $\alpha$-$Fe_2O_3$, the more pronounced were the diffraction lines related to $Fe_2TiO_5$ and $Al_{2-2x}Fe_{2x}TiO_5$. Dendritic pores were observed in the SEM micrographs of pure and $TiO_2$-alumina. However, this morphological feature was not observed in the $Fe_2O_3$ doped $TiO_2$-alumina. The change in pore geometry was attributed to the high density of $Fe_2O_3$ relative to $TiO_2$ and alumina. This resulted in a reduced critical solidification front velocity in the freezing of the solvent

(i.e. camphene), thus modifying the pore shape geometry. Light-gray regions with EDS signals associated with Ti, Fe, and Al were noticed in the micrographs of $TiO_2/Fe_2O_3$-containing samples, which were highly dispersed within the alumina structure. Cold crushing tests pointed out that the $Fe_2O_3$ doping led to materials with higher mechanical strength when compared to pure and $TiO_2$-alumina. This was attributed to $Fe_2O_3$ which improved the densification of alumina and inhibited the formation of cracks.

## ACKNOWLEDGMENTS

The authors thank the financial support from FAPEMIG, CAPES, and CNPq. We also appreciate Dra. Andréia Bicalho and the UFMG microscopy center for the technical support in the XRD and SEM tests, respectively. The authors are grateful to Almatis Brasil and Misses Daiana Sígolo and Susana Resende for providing the alumina and hematite powders used in this work. J.C. Diniz da Costa acknowledges the support given by the Australian Research Council (ARC) Future Fellowship Program (FT130100405).

## REFERENCES

[1] S. Deville, E. Saiz, A. Tomsia, Freeze casting of hydroxyapatite scaffolds for bone tissue engineering, Biomaterials, 27 (2006) 5480-5489.

[2] Z.-Y. Deng, H.R. Fernandes, J.M. Ventura, S. Kannan, J.M.F. Ferreira, Nano-$TiO_2$-coated unidirectional porous glass structure prepared by freeze drying and solution infiltration, J. Am. Ceram. Soc. 90 (2007) 1265-1268.

[3] R. Sepúlveda, A.A. Plunk, D.C. Dunand, Microstructure of $Fe_2O_3$ scaffolds created by freeze-casting and sintering, Mater. Lett. 142 (2015) 56-59.

[4] D.F. Souza, E.H.M. Nunes, D.S. Pimenta, D.C.L. Vasconcelos, J.F. Nascimento, W. Grava, M. Houmard, W.L. Vasconcelos, Synthesis and structural evaluation of freeze-cast porous alumina, Mater. Charact. 96 (2014) 183-195.

[5] W.L. Li, K. Lu, J.Y. Walz, Freeze casting of porous materials: Review of critical factors in microstructure evolution, Int. Mater. Rev.57 (2012) 37-60.

[6] C. Gaudillere, J. Garcia-Fayos, J.M. Serra, Enhancing oxygen permeation through hierarchically-structured perovskite membranes elaborated by freeze-casting, J. Mater. Chem. A 2 (2014) 3828-3833.

[7] Z. Xu, Q. Sun, F. Huang, Y. Pu, S. Pan, A.J. Ragauskas, Preparation and characteristics of cellulose nanowhisker reinforced acrylic foams synthesized by freeze-casting, RSC Adv. 4 (2014) 12148-12153.

[8] R.W. Trice, K.T. Faber, Role of lamellae morphology on the microstructural development and mechanical properties of small-particle plasma-sprayed alumina, J. Am. Ceram. Soc. 83 (2000) 889-896.

[9] R.S. Lima, B.R. Marple, Thermal spray coatings engineered from nanostructured ceramic agglomerated powders for structural, thermal barrier and biomedical applications: A review, J. Thermal Spray Technol. 16 (2007) 40-63.

[10] H.X. Peng, Z. Fan, J.R.G. Evans, Factors affecting the microstructure of a fine ceramic foam, Ceram. Int. 26 (2000) 887-895.

[11] A. R. Jamaludin, S. R. Kasim, A. K. Ismail, M.Z. Abdullah, Z.A. Ahmad, The effect of sago as binder in the fabrication of alumina foam through the polymeric sponge replication technique, J. Eur. Ceram. Soc. 35 (2015) 1905-1914.

[12] J. Bullon, M.P. Belleville, G.M. Rios, Preparation of gelatin formed-in-place membranes: effect of working conditions and substrates, J. Memb. Sci. 168 (2000) 159-165.

[13] F. Goncalves, C. Fernandes, M.N. de Pinho. White wine clarification by micro/ultrafiltration: effect of removed colloids in tartaric stability. Sep. Pur. Technol. 22-23 (2001) 423-429.

[14] C.R. Tanardi, A.F.M. Pinheiro, A. Nijmeijer, L. Winnubst, PDMS grafting of mesoporous gamma-alumina membranes for nanofiltration of organic solvents, J. Memb. Sci. 469 (2014) 471-477.

[15] T. Van Gestel, C. Vandecasteele, A. Buekenhoudt, C. Dotremont, J. Luyten, R. Leysen, B. Van der Bruggen, G. Maes, Alumina and titania multilayer membranes for nanofiltration: preparation, characterization and chemical stability, J. Memb. Sci. 207 (2002) 73-89.

[16] A. Darmawan, J. Motuzas, S. Smart, A. Julbe, J.C. Diniz da Costa, Binary iron cobalt oxide silica membrane for gas separation, J. Memb. Sci. 474 (2015) 32-38.

[17] B. Ballinger, J. Motuzas, S. Smart, J.C. Diniz da Costa, Palladium cobalt binary doping of molecular sieving silica membranes, J. Memb. Sci. 451(2014)185-191.

[18] C. Yacou, S. Smart, J.C. Diniz da Costa, Long term performance of a multi-tube cobalt oxide silica membrane at high temperatures for gas separation, Energy Environ. Sci. 5 (2012) 5820–5832.

[19] Z. Sadeghian, F. Zamani, S.N. Ashrafizadeh, Removal of oily hydrocarbon contaminants from wastewater by gamma-alumina nanofiltration membranes, Desal. Water Treat. 20 (2010) 80-85.

[20] M. Abbasi, M. Mirfendereski, M. Nikbakht, M. Golshenas, T. Mohammadi, Performance study of mullite and mullite-alumina ceramic MF membranes for oily wastewaters treatment, Desalination. 259 (2010) 169-178

[21] M.C. Duke, J. O'Brien-Abraham, N. Milne1, B. Zhu, J. Y. S. Lin, J.C. Diniz da Costa, Seawater desalination performance of MFI type membranes made by secondary growth, Sep. Pur. Technol. 68 (2009) 343-350

[22] M. Elma, D. Wang, C. Yacou, J.C. Diniz da Costa, Interlayer-free P123 carbonised template silica membranes for desalination with reduced salt concentration polarization, J. Mem. Sci. 475 (2015) 376-383

[23] M. Elma, D.K. Wang, C. Yacou, J. Motuzas, J.C. Diniz da Costa, High performance interlayer-free mesoporous cobalt oxide silica membranes for desalination applications, Desalination. 365 (2015) 308-315.

[24] Y. Zhang, K. Zhou, J. Zeng, D Zhang, Control of pore structures and sizes in freeze cast ceramics, Adv. App. Ceram. 112 (2013) 405-411.

[25] Y. Tang, Q. Miao, S. Qiu, K. Zhao, L. Hu, Novel freeze-casting fabrication of aligned lamellar porous alumina with a centrosymmetric structure, J. Eur. Ceram. Soc. 34 (2014) 4077-4082.

[26] S. Vijayan, R. Narasimman, K. Prabhakaran, Freeze gelcasting of naphthalene-in-aqueous alumina slurry emulsions for the preparation of macroporous alumina ceramics, Ceram. Int. 41 (2015) 1487-1494.

[27] C. Pekor, I. Nettleship, The effect of the molecular weight of polyethylene glycol on the microstructure of freeze-cast alumina, Ceram. Int. 40 (2014) 9171-9177.

[28] Y. Zhang, L. Hu, J. Han, Z. Jiang, Freeze casting of aqueous alumina slurries with glycerol for porous ceramics, Ceram. Int. 36 (2010) 617-621.

[29] A. Macchetta, I.G. Turner, C.R. Bowen, Fabrication of HA/TCP scaffolds with a graded and porous structure using a camphene-based freeze-casting method, Acta Biomater. 5 (2009) 1319-1327.

[30] K. Araki, J.W. Halloran, Room-temperature freeze casting for ceramics with nonaqueous sublimable vehicles in the naphthalene-camphor eutectic system, J. Am. Ceram. Soc. 87 (2004) 2014-2019.

[31] M. Li, F. Chen, Q. Shen, L. Zhang. Fabrication and thermal properties of $Al_2TiO_5/Al_2O_3$ composites, Mater. Sci. Poland. 28 (2010) 663-670.

[32] A.M.A. Silva, E.H.M. Nunes, D.F. Souza, D. Martens, J.C. Diniz da Costa, M. Houmard, W.L. Vasconcelos. Effect of titania addition on the properties of freeze-cast alumina samples. Ceram. Int. (in press) doi: 10.1016/j.ceramint.2015.04.132.

[33] M. Ishitsuka, T. Sato, T. Endo, M. Shimada, Synthesis and thermal-stability of aluminum titanate solid-solutions, J. Am. Ceram. Soc. 70 (1987) 69-71.

[34] D.S. Perera, Reaction-sintered aluminium titanate, J. Mater. Sci. Lett. 8 (1989) 1057-1059.

[35] V. Buscaglia, P. Nanni, Decomposition of $Al_2TiO_5$ and $Al_{2(1-x)}Mg_xTi_{(1+x)}O_5$ ceramics, J. Am. Ceram. Soc. 81 (1998) 2645-2653.

[36] I.J. Kim, Thermal stability of $Al_2TiO_5$ ceramics for new diesel particulate filter applications: A literature review, J. Ceram. Process. Res. 11 (2010) 411-418.

[37] V. Buscaglia, M. Alvazzi Delfrate, M. Leoni, C. Bottino, P. Nanni, The effect of $MgAl_2O_4$ on the formation kinetics of $Al_2TiO_5$ from $Al_2O_3$ and $TiO_2$ fine powders, J. Mater. Sci. 31 (1996) 1715-1724.

[38] F.C. Gennari, D.M. Pasquevich, Kinetics of the anatase rutile transformation in $TiO_2$ in the presence of $Fe_2O_3$, J. Mater. Sci. 33 (1998) 1571-1578.

[39] T.L. Lekanova, Y.I. Ryabkov, O.A. Sevbo, V.V. Viktorov, Phase relations in the systems $Al_2TiO_5$-$Fe_2O_3$, $Al_2O_3$-$TiO_2$-$Fe_2O_3$, and $Al_2TiO_5$-$Cr_2O_3$, Inorg. Mater. 40 (2004) 1191-1195.

[40] H. Joe, A.K. Vasudevan, G. Aruldhas, A.D. Damodaran, K.G.K. Warrier, FTIR as a tool to study high-temperature phase formation in sol-gel aluminium titanate, J. Solid State Chem. 131 (1997) 181-184.

[41] A. Adamczyk, E. Długon, The FTIR studies of gels and thin films of $Al_2O_3$-$TiO_2$ and $Al_2O_3$-$TiO_2$-$SiO_2$ systems, Spectrochim. Acta Part A. 89 (2012) 11-17.

[42] M.G.Naseri, E.B. Saion, A.H. Shaari, M. Hashim, M. Goodarz Naseri, H. Abbastabar Ahangar, M. Hashim, Simple synthesis and characterization of cobalt ferrite nanoparticles by a thermal treatment method, J. Nanomater. 2010 (2010) 1-8.

[43] C. Lenser, A. Kalinko, A. Kuzmin, D. Berzins, J. Purans, K. Szot, R. Waser, R. Dittmann, Spectroscopic study of the electric field induced valence change of Fe-defect centers in $SrTiO_3$, Phys. Chem. Chem. Phys. 13 (2011) 20779-20786.

[44] P. Tarte, Infrared spectra of inorganic aluminates and characteristic vibrational frequencies of $AlO_4$ tetrahedra and $AlO_6$ octaedra, Spectrochim. Acta Part A. 23 (1967) 2127-2143.

[45] M. Crişan, M. Zaharescu, V.D. Kumari, M. Subrahmanyam, D. Crişan, N. Drăgan, M. Răileanu, M. Jitianu, A. Rusu, G. Sadanandam, J.K.Reddy, Sol-gel based alumina powders with catalytic applications, Appl. Surf. Sci. 258 (2011) 448-455.

[46] F.I. Hurwitz, H. Guo, R.B. Rogers, E.J. Sheets, D.R. Miller, K.N. Newlin, M.K. Shave, A.R. Palczer, M.T. Cox, Influence of Ti addition on boehmite-derived aluminum silicate aerogels: Structure and properties, J. Sol-Gel Sci. Technol. 64 (2012) 367-374.

[47] A. Macchetta, I.G. Turner, C.R. Bowen, Fabrication of HA/TCP scaffolds with a graded and porous structure using a camphene-based freeze-casting method, Acta Biomater. 5 (2009) 1319-1327.

[48] K. Araki, J.W. Halloran, Room-temperature freeze casting for ceramics with nonaqueous sublimable vehicles in the naphthalene-camphor eutectic system, J. Am. Ceram. Soc. 87 (2004) 2014-2019.

[49] J. Han, C. Hong, X. Zhang, J. Du, W. Zhang, Highly porous $ZrO_2$ ceramics fabricated by a camphene-based freeze-casting route: Microstructure and properties, J. Eur. Ceram. Soc. 30 (2010) 53-60.

[50] E.C. Hammel, O.L.-R. Ighodaro, O.I. Okoli, Processing and properties of advanced porous ceramics: An application based review, Ceram. Int. 40 (2014) 15351-15370.

[51] Y. Chino, D.C. Dunand, Directionally freeze-cast titanium foam with aligned, elongated pores, Acta Mater. 56 (2008) 105-113.

[52] P. Casses, M.A. Azouniaidi, A general theoretical approach to the behavior of foreign particles at advancing solid-liquid interfaces, Adv. Colloid Interface. 50 (1994) 103-120.

[53] I.B. de Arenas, O. Gil, Synthesis and properties of in situ $Al_2TiO_5/Al_2O_3$ composite, J. Mater. Process. Technol. 143-144 (2003) 838-842.

[54] H.R. Rezaie, R. Naghizadeh, N. Farrokhnia¸ S. Arabi¸ M. Sobhani, The effect of $Fe_2O_3$ addition on tialite formation, Ceram. Int. 35 (2009) 679-684.

[55] H.P. Cahoon, C.J. Christensen, Sintering and grain growth of alpha-alumina, J. Am. Ceram. Soc. 39 (1956) 337-344.

[56] G. Rossi, J.E. Burke, Influence of additives on the microstructure of sintered $Al_2O_3$, J. Am. Ceram. Soc. 56 (1973) 654-659.

[57] Y.-M. Kim, S.-H.Hong, D.-Y. Kim, Anisotropic abnormal grain growth in $TiO_2/SiO_2$-doped alumina, J. Am. Ceram. Soc. 83 (2000) 2809-2812.

[58] R.D. Bagley, I.B. Cutler, D.L. Johnson, Effect of $TiO_2$ on initial sintering of $Al_2O_3$, J. Am. Ceram. Soc. 53 (1970) 136-141.

[59] J. Tartaj, G.L. Messing, Effect of the addition of alpha-$Fe_2O_3$ on the microstructural development of boehmite-derived alumina, J. Mater. Sci. Lett. 16 (1997) 168-170.

## FIGURE CAPTIONS

**- Figure 1:** Particle size distribution of the starting powders used in this work.

**- Figure 2:** XRD patterns of samples prepared in this study. (I) α-$Al_2O_3$; (II) α-$Al_2O_3$ + $TiO_2$ (4 wt%); (III) α-$Al_2O_3$ + $TiO_2$ (4 wt%) + α-$Fe_2O_3$ (2.5 wt%); (IV) α-$Al_2O_3$ + $TiO_2$ (4 wt%) + α-$Fe_2O_3$ (5 wt%); (V) α-$Al_2O_3$ + $TiO_2$ (4 wt%) + α-$Fe_2O_3$ (7.5 wt%); (VI) α-$Al_2O_3$ + $TiO_2$ (4 wt%) + α-$Fe_2O_3$ (10 wt%). The JCPDS file numbers 00-010-0173, 00-041-0258, 00-076-1158, and 00-076-1157 were used as reference for α-$Al_2O_3$, β-$Al_2TiO_5$, $Fe_2TiO_5$, and $Al_{2-2x}Fe_{2x}TiO_5$, respectively.

- **Figure 3:** FTIR spectra of samples used in this work. (I) α-$Al_2O_3$ + $TiO_2$ (4 wt%); (II) α-$Al_2O_3$ + $TiO_2$ (4 wt%) + α-$Fe_2O_3$ (2.5 wt%); (III) α-$Al_2O_3$ + $TiO_2$ (4 wt%) + α-$Fe_2O_3$ (5 wt%); (IV) α-$Al_2O_3$ + $TiO_2$ (4 wt%) + α-$Fe_2O_3$ (7.5 wt%); (V) α-$Al_2O_3$ + $TiO_2$ (4 wt%) + α-$Fe_2O_3$ (10 wt%). The spectra were normalized using the band at 645 $cm^{-1}$ as reference.

- **Figure 4:** SEM micrographs of $TiO_2$-containing alumina. The scale bars correspond to 200 and 20 μm in (A) and (B), respectively.

- **Figure 5:** SEM micrographs of $TiO_2$/$Fe_2O_3$-containing alumina. Sample prepared with a 10 wt% $Fe_2O_3$ loading. The scale bars correspond to 100 and 20 μm in (A) and (B), respectively.

- **Figure 6:** SEM micrographs and EDS spectra of $TiO_2/Fe_2O_3$-containing alumina. Sample prepared with a 10 wt% $Fe_2O_3$ loading. The scale bar in the micrograph corresponds to 20 μm.

- **Figure 7:** μ-CT images of materials obtained in this work.

- **Figure 8:** Porosity and shrinkage of samples prepared in this study as a function of the $Fe_2O_3$ loading. The dotted lines are used only as a guide to the eyes.

- **Figure 9:** Cold crushing strength as a function of the $Fe_2O_3$ loading and porosity. The dotted lines are used only as a guide to the eyes.

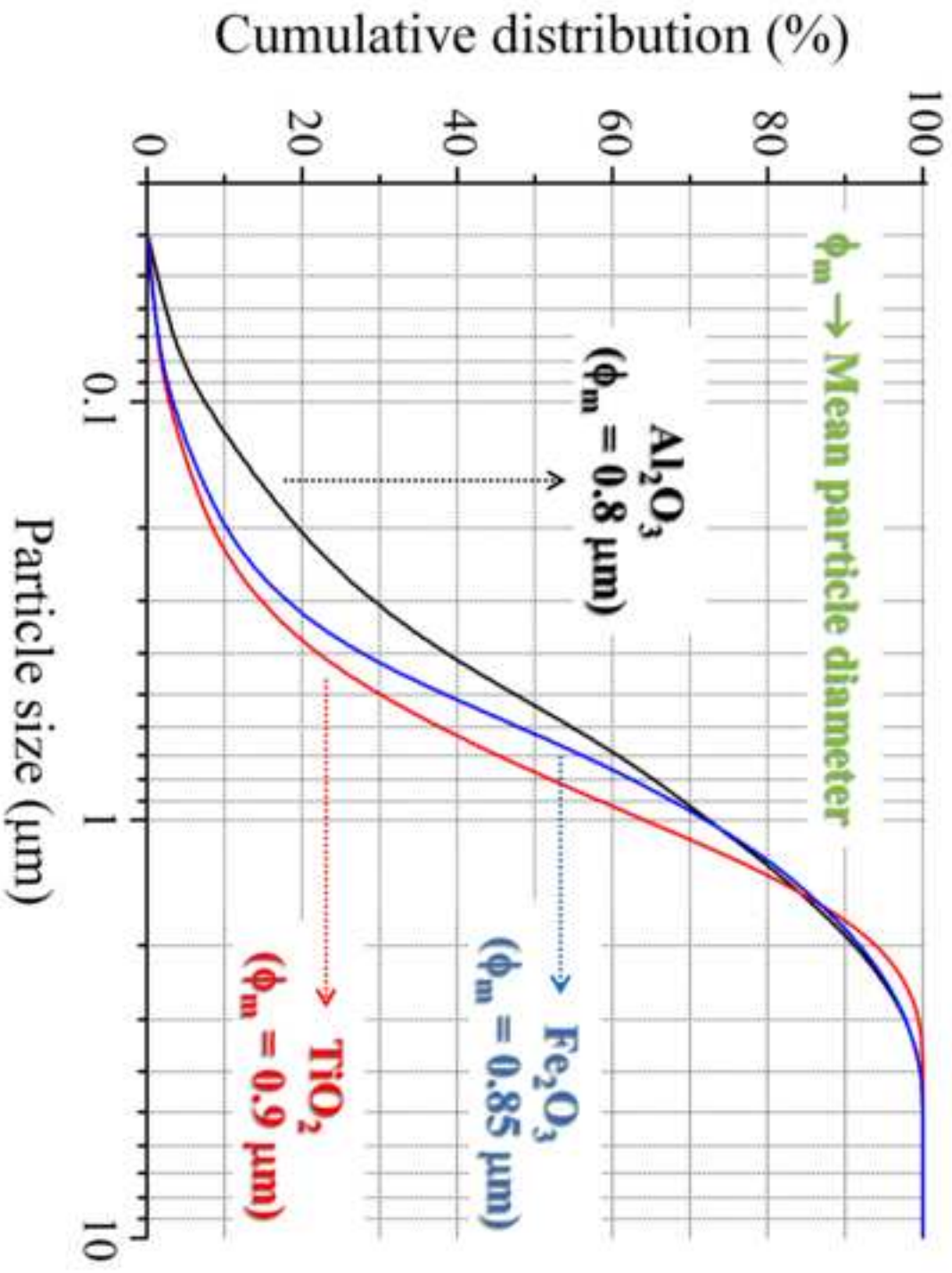


Figure 1

Figure 2

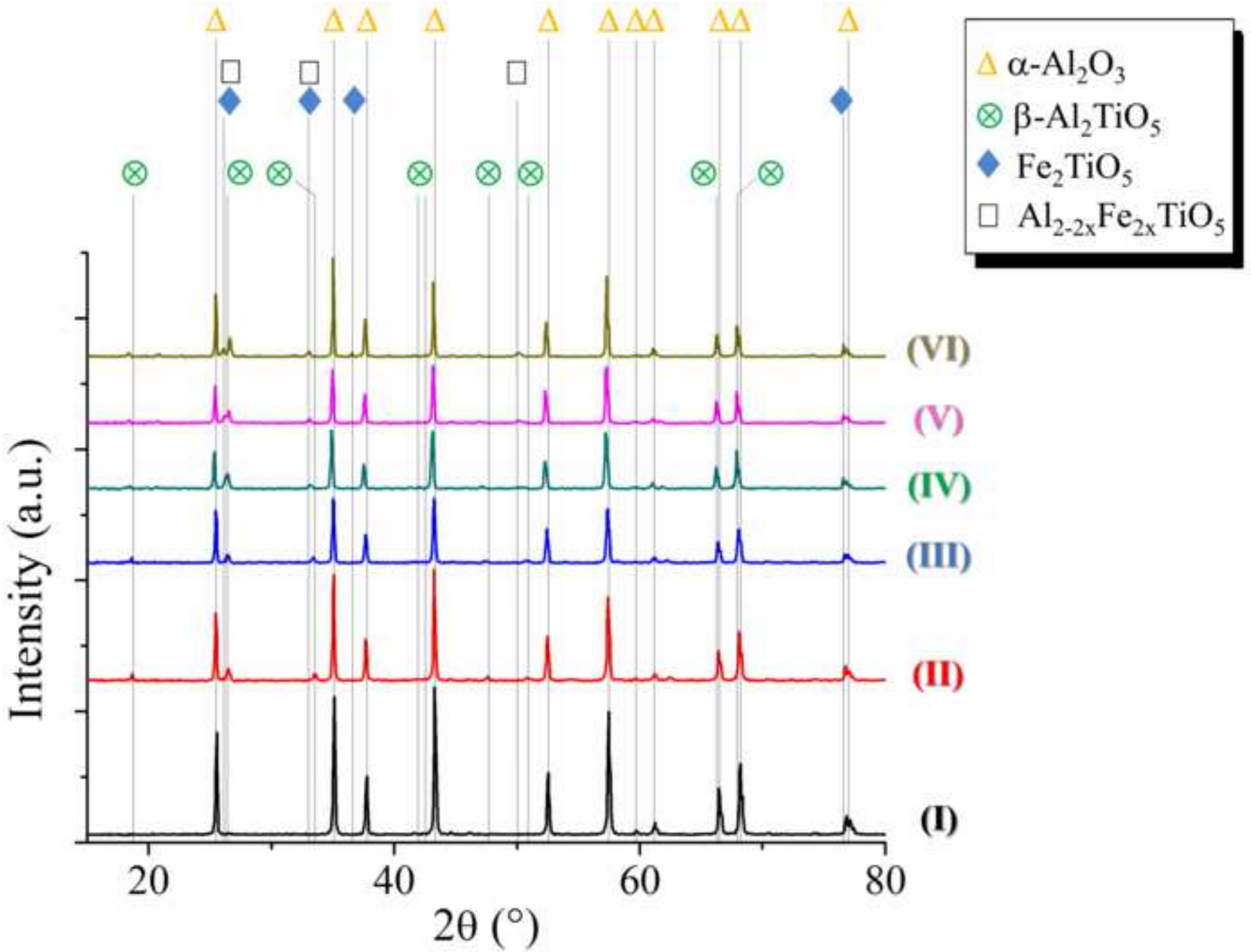

Figure 3

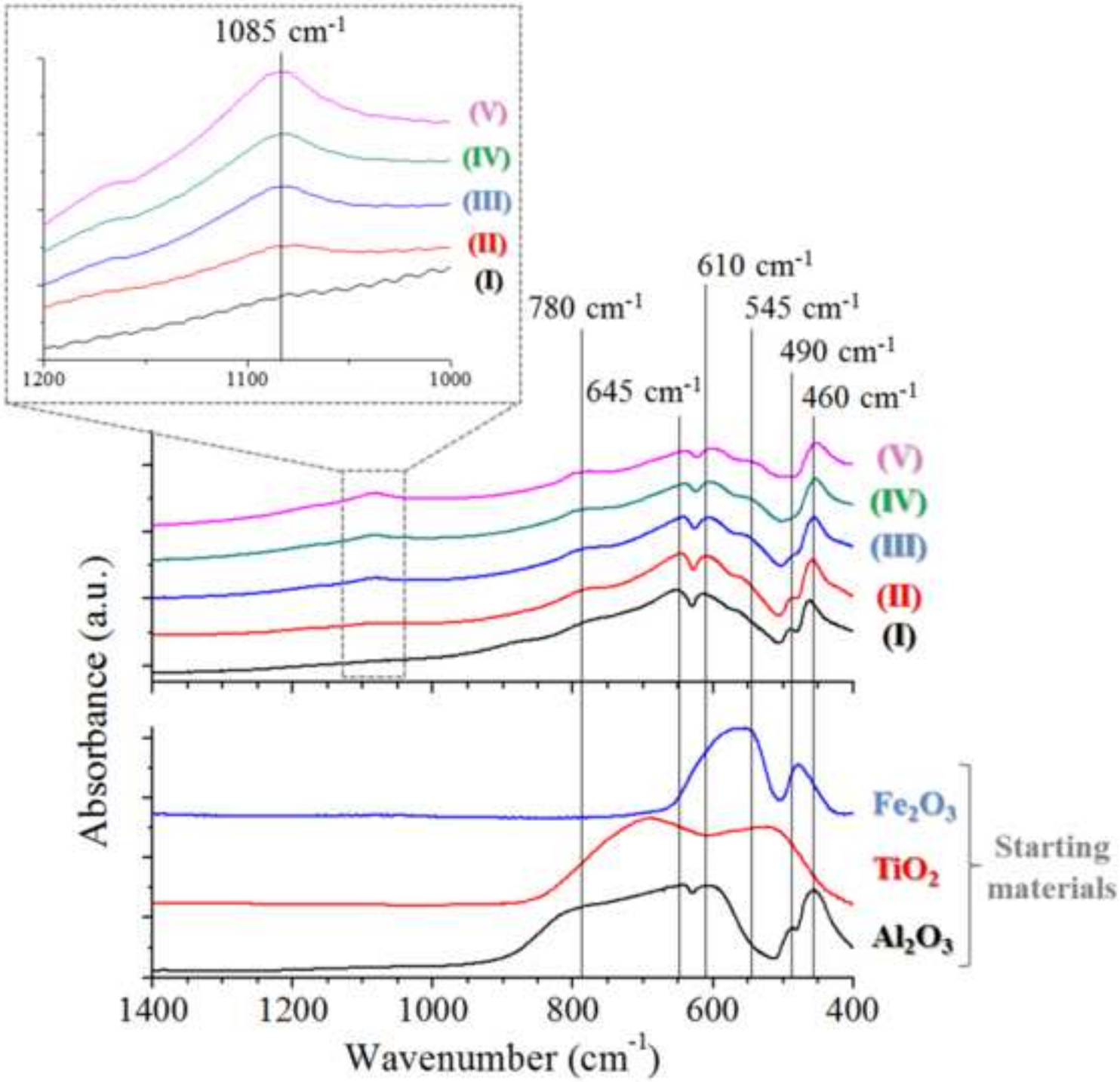

Figure 4

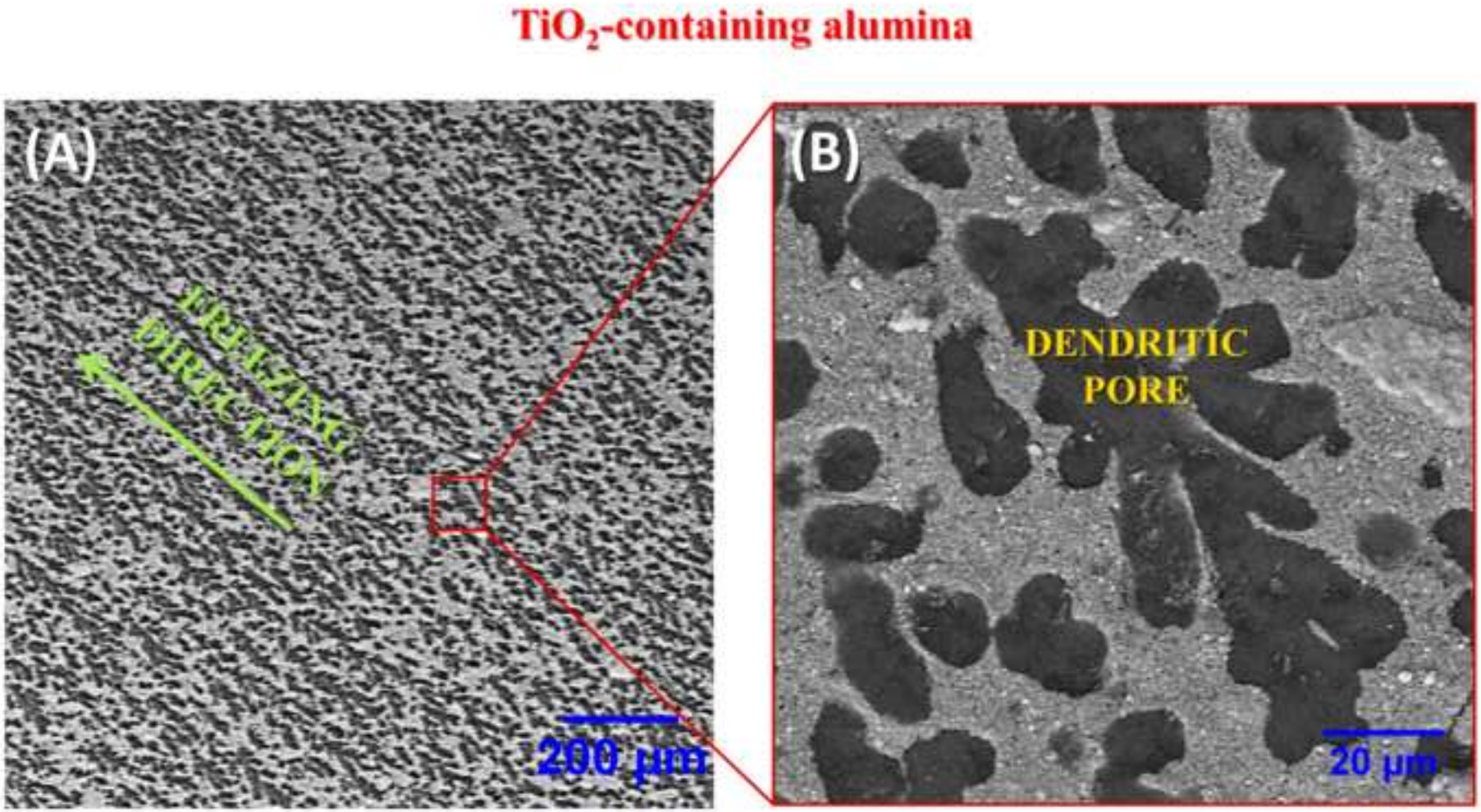

Figure 5

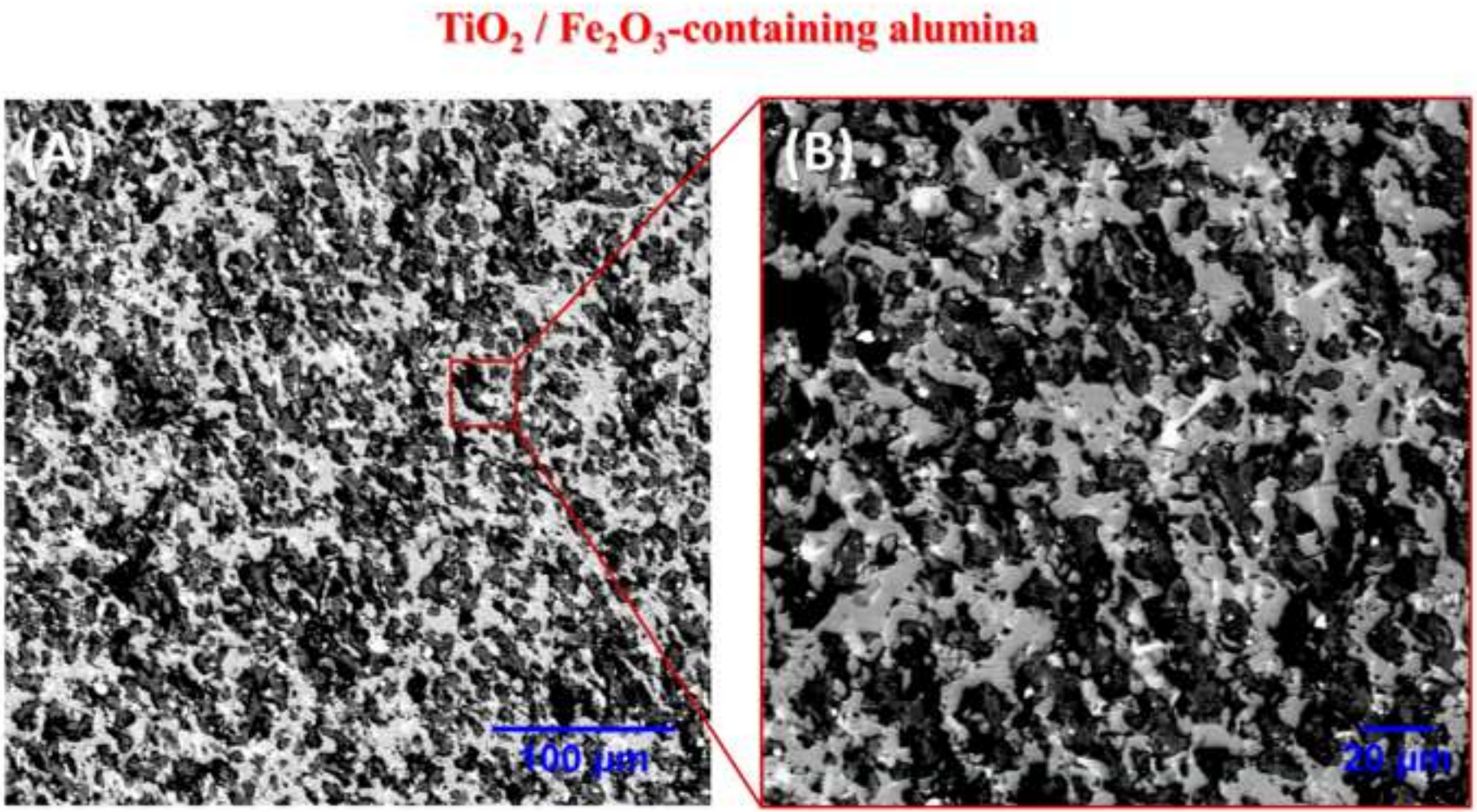

Figure 6

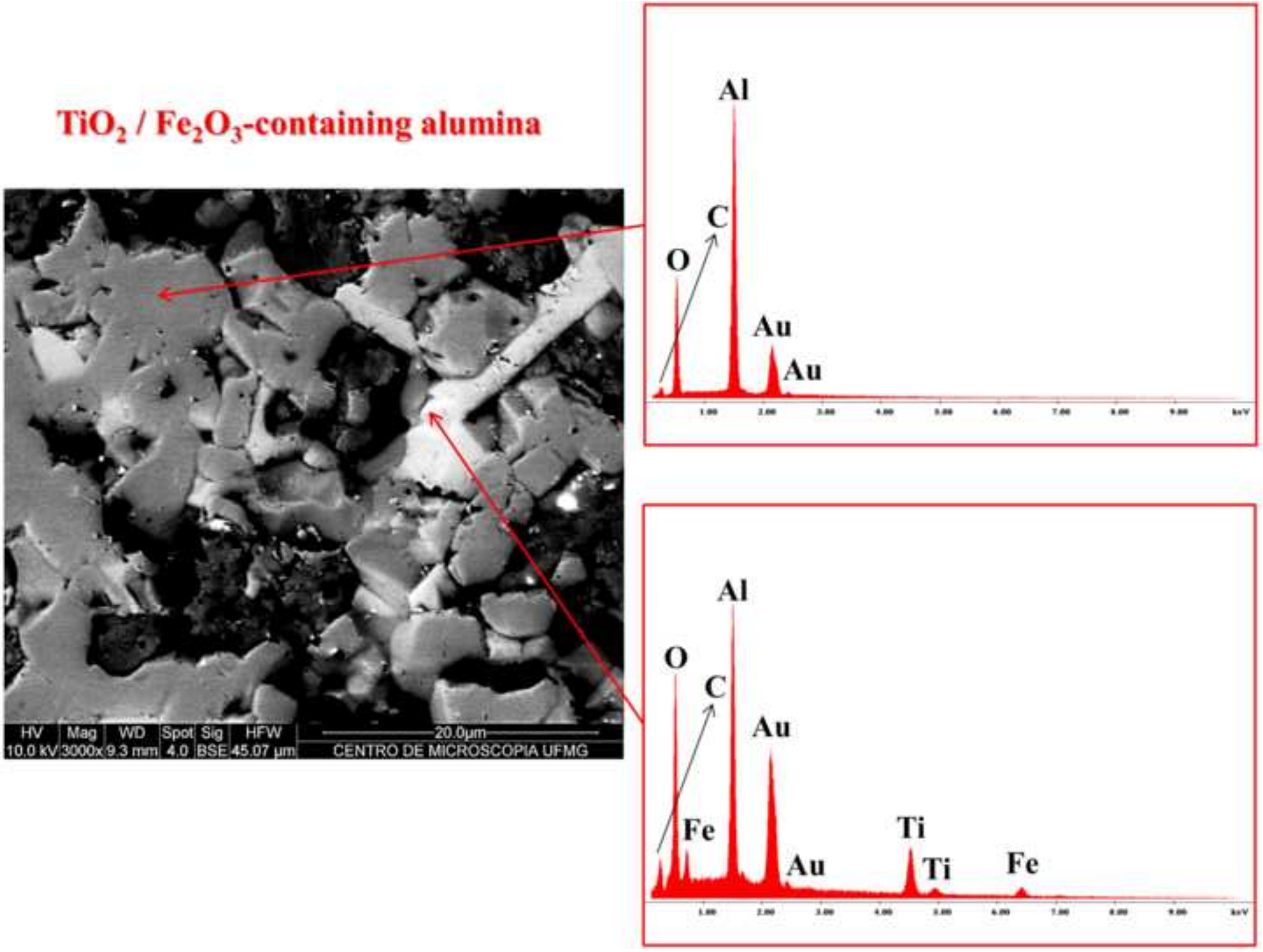

Figure 7

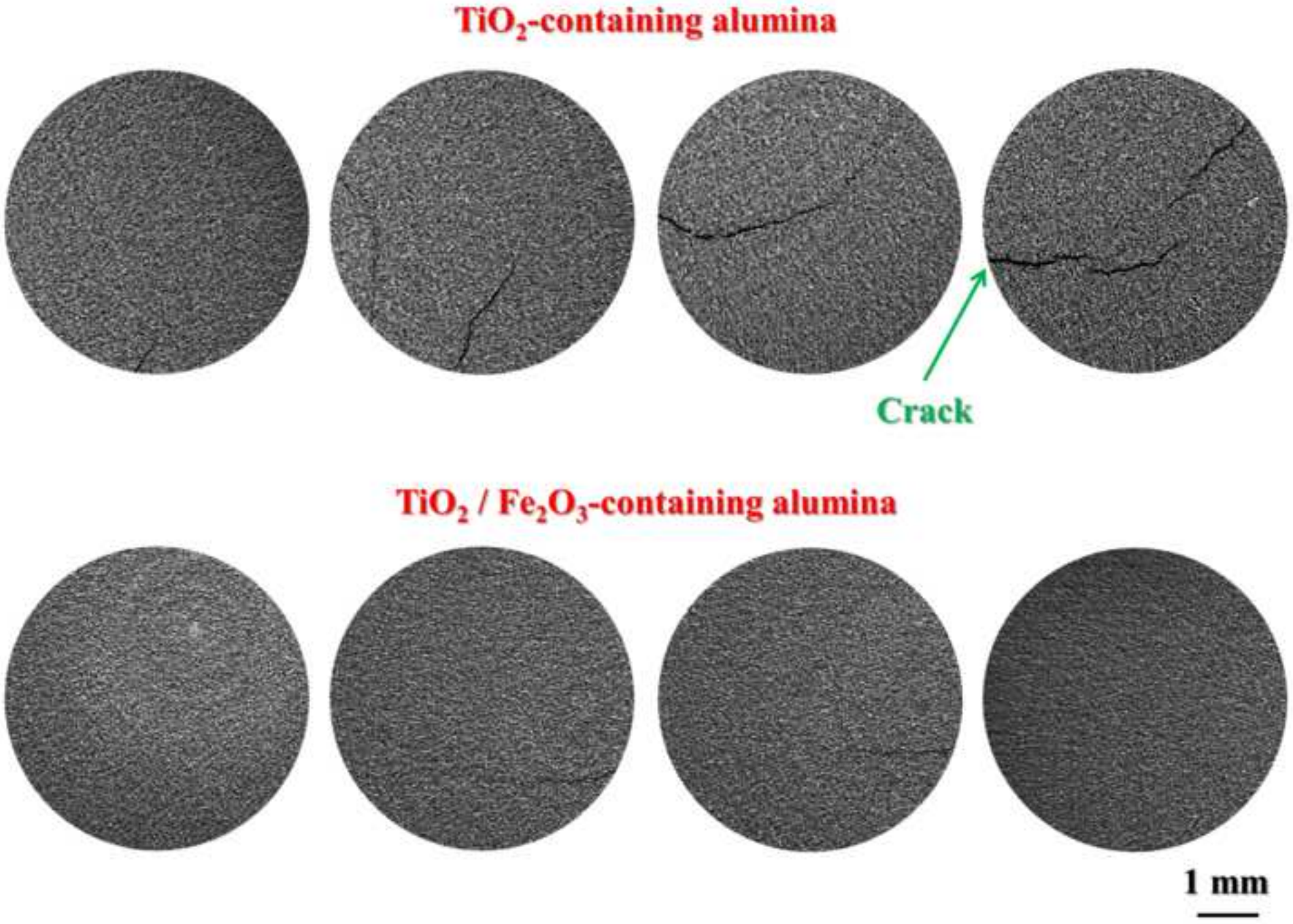

Figure 8

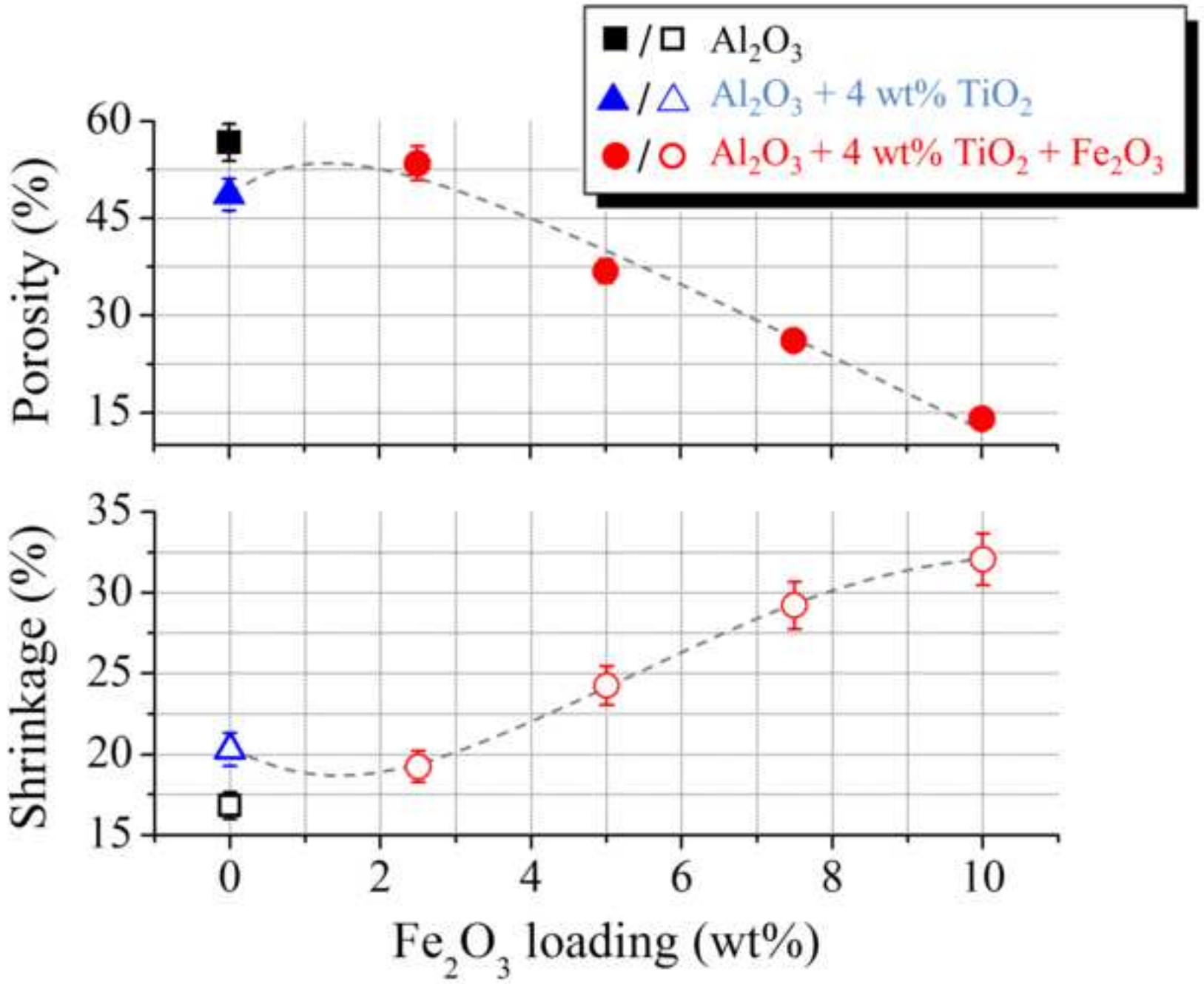

Figure 9